

# RESLS: Region and Edge Synergetic Level Set Framework for Image Segmentation

Weihsang Zhang<sup>1</sup>, Xue Wang<sup>2</sup>, *Senior Member, IEEE*, Wei You, Junfeng Chen, Peng Dai<sup>3</sup>, and Pengbo Zhang<sup>4</sup>

**Abstract**—The active contour models with level set evolution have been visited with a vast number of methods for image segmentation. They can be mainly classified into region-based and edge-based models, and it has been validated that the hybrid variants combining both region and edge information can improve the segmentation performance. However, to the best of our knowledge, the theoretical foundation of collaboration mechanism between the region and the edge information is limited. Specifically, most existing hybrid models are just combining all the energy terms together, resulting in great challenges of choosing an appropriate weight coefficient for each term and accommodating different modalities of imaging. To overcome these difficulties, this paper proposes a region and edge synergetic level set framework named RESLS. It provides an approach to construct new hybrid level set models using a normalized intensity indicator function that allows the region information easily embedding into the edge-based model. In this case, the energy weights of region and edge terms can be constrained by the global optimization condition deduced from the framework. Some representative as well as state-of-the-art models are taken as examples to demonstrate the generality of our method. The experiments validate that under the guidance of the optimization condition, the weighting parameter of each term can be reliably chosen. Meanwhile, the segmentation accuracy, robustness, and computational efficiency of RESLS can be improved compared with its component models.

**Index Terms**—Image segmentation, active contour, level set, region and edge, hybrid models.

## I. INTRODUCTION

IMAGE segmentation is an effective analysis tool in the field of pattern recognition and computer vision. It has been used in a wide range such as medical image analysis [1], [2], intelligent transportation [3], [4], defect detection [5], satellite image processing [6], etc. With the development of artificial intelligence, a variety of image segmentation technologies have been proposed in recent years, especially the advances using deep neural networks for semantic segmentation [7]–[11] and scene parsing [12]–[15]. These learning based methods have made a significant breakthrough

in searching statistical features from large scale datasets. However, the traditional methods using the specific image information [16], [17] are more competent in processing detailed patterns. Especially, in the case of insufficient samples, the image segmentation by traditional models is still a fast and effective solution. Moreover, in many challenging scenarios, it is difficult to solve the problem only using a single method. The current research trend is to combine the machine learning and traditional models to obtain more refined results, such as the contributions in Refs. [18]–[21]. It can be seen that the traditional methods still play an important role in the era of machine learning, which should be paid more attention.

Among these methods, the active contour models (ACMs) have been widely used since the 1990s. The curve evolution theory was invoked into ACMs by solving partial differential equations of the corresponding evolution curves [22]. The earliest ACM was proposed by Kass *et al.* [23], which uses the parametric method to describe the evolution curve, named Snakes. However, the Snakes model suffers from a lot of drawbacks such as low robustness and accuracy. A great number of strategies have been proposed to remedy the defects of Snakes, such as balloon force Snakes [24], gradient vector flow Snakes [25], etc. Nevertheless, due to the inevitable explicit formulation of parametric evolution curve, the ACMs still face great challenges in numerical computation and topological changes.

To overcome the above difficulties, the level set method (LSM) was introduced independently by Caselles *et al.* [26] and Malladi *et al.* [27] in the context of ACMs. The LSM uses an implicit expression of level set function (LSF) instead of parametric evolution curve. Therefore, the numerical computation can be performed on a fixed Cartesian grid without parameterizing the points on the curve. Moreover, the LSF can represent contours with complex topology and efficiently handle topological changes, such as splitting and merging. However, the applications of conventional LSM are plagued with the irregularities of LSF developed during level set evolution, resulting in numerical errors and instability of image segmentation. To handle these problems, Bresson *et al.* [28] proposed a fast global minimization of the ACMs with a dual formulation that avoids re-initializing the LSF. Li *et al.* [29] proposed a distance regularization term to maintain the regularity and stability of LSF. Afterwards, they extended their work by presenting a double-well potential for the regularization term in Ref. [30], which is very typical and has been widely used up to now.

Manuscript received April 16, 2018; revised December 2, 2018 and April 22, 2019; accepted July 6, 2019. Date of publication July 17, 2019; date of current version September 12, 2019. This work was supported in part by the National Key Research and Development Program of China under Grant 2018YFB2003500 and Grant 2018YFB2003200 and in part by the National Natural Science Foundation of China under Grant 61472216. The associate editor coordinating the review of this manuscript and approving it for publication was Prof. Jingyi Yu. (*Corresponding author: Xue Wang.*)

The authors are with the State Key Laboratory of Precision Measurement Technology and Instruments, Department of Precision Instrument, Tsinghua University, Beijing 100084, China (e-mail: zwh15@mails.tsinghua.edu.cn; wangxue@mail.tsinghua.edu.cn).

Digital Object Identifier 10.1109/TIP.2019.2928134

The LSM can be mainly classified into two basic models: region-based level set (RLS) [31] and edge-based level set (ELS) [26], which have their own strengths and weaknesses for different situations. The RLS is suitable for images in which there is an obvious difference of grayscale distribution between the object and background. The curve evolution is robust to the initialization of LSF. However, the RLS generally suffers from low accuracy on images with intensity inhomogeneity and low computational efficiency. In contrast, the ELS is suitable for images with obvious boundaries between the object and background and achieves relatively high computation speed compared with RLS. However, The ELS is inapplicable to the object with weak boundaries, and it is usually sensitive to the initialization of LSF.

To improve the performance of LSM in more challenging cases, many other level set models have been presented. For instance, Lankton and Tannenbaum [32] introduced a framework that allows any RLS models to be re-formulated in a local way for segmenting objects with heterogeneous features. Mesadi *et al.* [33] proposed a disjunctive normal RLS for image segmentation. This method can be regarded as an open framework which allows the use of different shape priors and appearance models. Akram *et al.* [34] proposed a novel ELS method based on the difference of Gaussians (DoG) to segment intensity inhomogeneous images. The DoG is used as an edge indicator parameter, which acts as a feature enhancement tool to enhance the edges of an image. Khadidos *et al.* [17] presented a LSM based on local edge features in which the energy terms are weighted in accordance with their relative importance in detecting boundaries.

To take the advantages of both RLS and ELS models, some researchers have proposed hybrid level set models by combining both region and edge information. For example, Appia and Yezzi [35] proposed a region-based model with a global edge-based constraint, which automatically achieves local optimality with respect to an edge fitting criterion. Balla-Arabé *et al.* [36] presented a GPU accelerated LSM which simultaneously uses region, edge, and 2D histogram information to efficiently segment objects of interest. Tian *et al.* [37] proposed a hybrid model with an edge-related term derived from the image gradient and a region-based term using both local and global statistical information. Ali *et al.* [38] presented a variational model for segmentation of images with intensity inhomogeneity. The fitting energies are based on regions and edges enhanced quantities from multiplicative and difference images, respectively.

However, to the best of our knowledge, the theoretical foundation of the existing hybrid LSM is insufficient and limited. The collaboration mechanism between the region and edge information has not been clearly revealed. More specifically, many newly proposed hybrid level set models usually adopt the brute force way of just adding all the energy terms together [39], which might cause two defects. Firstly, it is difficult to choose an appropriate weighting factor for each energy term because of two reasons:

- 1) As we all know, for most level set models, the region information usually works in a global manner, while the edge information generally acts in a local one [40].

Since we usually cannot find out the intensity distribution in advance, if we configure the parameters of region and edge terms without any constraint, the segmentation result might be trapped into local minima.

- 2) Since there is no quantitative description of the relationship between the region and edge information, it is difficult to estimate how much each energy term contributes to the whole energy functional, because the energy value of the region term is usually positively correlated with the area of the object, while the energy value of the edge term is often positively correlated with the boundary length of the target. Therefore, the energy values of these two terms might vary greatly. If the configuration of their weighting parameters is not appropriate, the region or the edge term may not work effectively.

Secondly, the energy weights of most existing hybrid models are usually determined by experience or experiment, which makes it difficult to accommodate different objects and modalities.

To address the above shortcomings, we propose a region and edge synergetic level set framework, named RESLS, which provides an approach to construct new hybrid level set models using a normalized intensity indicator function. The indicator function makes it easy to integrate the region information into the edge-based model. Meanwhile, the energy weights of region and edge terms can be reliably chosen under the guidance of the global optimization condition deduced from the proposed framework. Moreover, since the region and edge information is intrinsically combined, the RESLS enables improvements of segmentation performance compared with the models which are used to construct the framework. Firstly, the RESLS achieves relatively high segmentation accuracy in objects with intensity inhomogeneity and weak boundaries. Secondly, it is robust to the initialization of LSF. Thirdly, the computational efficiency can be improved in some cases. Some representative as well as state-of-the-art models are taken as examples to demonstrate the generality of our framework.

The remainder of this article is organized as follows. Section II briefly introduces some representative and state-of-the-art level set models which are related to the proposed method. Section III describes the RESLS framework in detail and deduces the global optimization condition that constrains the energy weights of region and edge terms. The generality and implementation of RESLS are also discussed in this section. Section IV shows the experimental results with the related works introduced in section II to demonstrate the performance of our method. Finally, section V makes a brief conclusion of the overall paper.

## II. PRELIMINARY

In this section, we firstly define the mathematical notations for level set models, and then introduce some important works that are related to our RESLS framework. It is worth noting that some additional regularization terms may be left out for a convenient expression. For an image  $I(\mathbf{x})$  on the image domain  $\Omega$ , where  $\mathbf{x} \in \Omega$  is a point of the image, the LSM defines an

energy functional  $E(\phi)$  with respect to a LSF  $\phi = \phi(\mathbf{x}, t) : R^n \times [0, t] \rightarrow R, t \geq 0$ . When the zero level contour  $\phi(\mathbf{x}, t) = 0$  moves to the object boundary, the partial differential of  $E(\phi)$  is expected to be 0. In this paper, we always use the LSF that takes negative values inside and positive values outside the zero level contour, so that the energy functional can always be minimized when  $\partial E(\phi)/\partial \phi = 0$ .

One of the most typical edge-based level set models is proposed by Li *et al.* [30], named distance regularized level set evolution (DRLSE), which is inspired by the geometric ACM proposed by Caselles *et al.* [26]. The energy functional of DRLSE can be expressed as

$$E_{DRLSE}(\phi) = \lambda_1 \int_{\Omega} g\delta(\phi) |\nabla \phi| d\mathbf{x} + \lambda_2 \int_{\Omega} gH(-\phi) d\mathbf{x} \quad (1)$$

where  $\lambda_1 > 0$  is the weight of edge term that computes the line integral of function  $g$  along the zero level contour.  $H$  is the Heaviside function.  $\delta$  is the Dirac delta function, which is the derivative of  $H$ .  $g$  is a well-known normalized edge indicator function defined as

$$g(\mathbf{x}) = \frac{1}{1 + |\nabla I(\mathbf{x})|^2} \quad (2)$$

$\lambda_2$  in Eqn.(1) is the weight of driving term that drives the evolution curve to the boundary of the object. Note that  $\lambda_2 > 0$  if the zero level contour is placed outside the object and  $\lambda_2 < 0$  if inside. For brevity, we omit the Gaussian filter usually used in Eqn.(2).

The earliest region-based level set model was proposed by Chan and Vese [31], named CV model, whose energy functional can be formulated as

$$E_{CV}(\phi) = \sum_{i=1}^2 v_i \int_{\Omega} |I(\mathbf{x}) - c_i|^2 M_i^{\mathbf{x}} d\mathbf{x} \quad (3)$$

where  $v_i > 0$  ( $i = 1, 2$ ) are the energy weights.  $c_1$  and  $c_2$  are two constants that approximate the image intensity inside and outside the zero level contour, respectively.  $M_1^{\mathbf{x}} = H[-\phi(\mathbf{x}, t)]$  and  $M_2^{\mathbf{x}} = 1 - H[-\phi(\mathbf{x}, t)]$ , similarly hereinafter.

In fact, the CV model is a piecewise constant model that is not suitable for images with intensity inhomogeneity. To address this problem, Li *et al.* [41] proposed the local binary fitting (LBF) model with its energy functional defined as

$$E_{LBF}(\phi) = \sum_{i=1}^2 \gamma_i \int_{\Omega} \int_{\Omega} K(\mathbf{x}, \mathbf{y}) |I(\mathbf{y}) - u_i(\mathbf{x})|^2 M_i^{\mathbf{y}} d\mathbf{y} d\mathbf{x} \quad (4)$$

where  $\gamma_i > 0$  ( $i = 1, 2$ ) are the energy weights.  $K(\mathbf{x}, \mathbf{y})$  is a type of kernel function and similarly hereinafter.  $u_1(\mathbf{x})$  and  $u_2(\mathbf{x})$  are two functions that locally approximate the image intensity inside and outside the zero level contour at the point  $\mathbf{x}$ , respectively.

Li *et al.* [42] further proposed a region-based model using local intensity clustering (LIC) to simultaneously segment heterogeneous images and estimate the bias field. The energy functional of LIC model is expressed as

$$E_{LIC}(\phi) = \sum_{i=1}^2 \int_{\Omega} \int_{\Omega} K(\mathbf{x}, \mathbf{y}) |I(\mathbf{y}) - b(\mathbf{x})m_i|^2 M_i^{\mathbf{y}} d\mathbf{y} d\mathbf{x} \quad (5)$$

where  $b(\mathbf{x})$  represents the bias field at the point  $\mathbf{x}$ .  $m_1$  and  $m_2$  are two variables that approximate the true image intensity (without bias field) inside and outside the zero level contour, respectively.

For more recent works, Zhang *et al.* [43] proposed the local statistical active contour model (LSACM) in which the objects with intensity inhomogeneity are modeled as Gaussian distributions of disparate means and variances. The energy functional of LSACM can be formulated as

$$E_{LSACM}(\phi) = \sum_{i=1}^2 \int_{\Omega} \int_{\Omega} K(\mathbf{x}, \mathbf{y}) \left[ \log(\sigma_i) + \frac{|I(\mathbf{y}) - b(\mathbf{x})m_i|^2}{2\sigma_i^2} \right] M_i^{\mathbf{y}} d\mathbf{y} d\mathbf{x} \quad (6)$$

where  $\sigma_1$  and  $\sigma_2$  respectively denote the standard deviation of Gaussian distribution inside and outside the zero level contour. The other notations are the same as in Eqn.(5).

To handle the images suffered from severe intensity inhomogeneity, Min *et al.* [44] proposed a level set model based on local approximation of Taylor expansion (LATE), which is able to approximate the variation degree of intensity inhomogeneity in a nonconvex manner. The energy functional of LATE model can be defined as

$$E_{LATE}(\phi) = \sum_{i=1}^2 \int_{\Omega} \int_{\Omega} K(\mathbf{x}, \mathbf{y}) |I(\mathbf{y}) - LIM_i(\mathbf{y}) - b'(\mathbf{x})e_i|^2 M_i^{\mathbf{y}} d\mathbf{y} d\mathbf{x} \quad (7)$$

where  $b'(\mathbf{x})$  denotes the first derivative of the bias field  $b(\mathbf{x})$ .  $e_1$  and  $e_2$  are two variables which are correlated with the features inside and outside the zero level contour, respectively.  $LIM_1(\mathbf{y})$  and  $LIM_2(\mathbf{y})$  are local intensity means in the object and background regions centered at  $\mathbf{y}$ .

To overcome the difficulty of the unknown noise distribution of an image, Niu *et al.* [45] presented an anti-noise model, named RLSF, by introducing a local similarity factor based on the spatial distance within a local window. The energy functional of RLSF model is defined as

$$E_{RLSF}(\phi) = \sum_{i=1}^2 \kappa_i \int_{\Omega} \left[ \int_{(\mathbf{y} \in N_{\mathbf{x}}) \neq \mathbf{x}} \frac{|I(\mathbf{y}) - u_i(\mathbf{x})|^2}{d(\mathbf{x}, \mathbf{y})} d\mathbf{y} \right] M_i^{\mathbf{x}} d\mathbf{x} \quad (8)$$

where  $\kappa_i > 0$  ( $i = 1, 2$ ) are the energy weights.  $d(\mathbf{x}, \mathbf{y})$  represents the spatial Euclidean distance between two pixels  $\mathbf{x}$  and  $\mathbf{y}$ .  $N_{\mathbf{x}}$  is a local window defined as a neighborhood of pixels surrounding the point  $\mathbf{x}$ .  $u_i(\mathbf{x})$  is the same as in Eqn.(4).

### III. THE RESLS FRAMEWORK

#### A. Motivations of RESLS

To take the advantages of both region and edge information, a primary idea of constructing hybrid level set models is to directly add all the region and edge terms together using some existing models. Taking the DRLSE and CV models as an



example, the energy functional of the hybrid model can be formulated by combining Eqn.(1) and Eqn.(3).

$$E_H(\phi) = \lambda_1 \int_{\Omega} g\delta(\phi) |\nabla\phi| d\mathbf{x} + \lambda_2 \int_{\Omega} gH(-\phi)d\mathbf{x} + \sum_{i=1}^2 v_i \int_{\Omega} |I(\mathbf{x}) - c_i|^2 M_i^{\mathbf{x}} d\mathbf{x} \quad (9)$$

This is a nonconvex function because the CV model works in a global manner, while the DRLSE model acts in a local one. As a consequence, the segmentation result might be trapped into local minima during the level set evolution.

Moreover, it can be seen that four energy weights should be appropriately determined for a specific image, which brings a great challenge since it is difficult to estimate how much each energy term contributes to the whole energy functional  $E_H(\phi)$ . The energy values of the four terms in Eqn.(9) might vary to a great extent. If these weighting parameters are set inappropriately, some of the energy terms may not work in an effective way. In this case, the energy weights should be determined by experience or experiment, which makes it difficult to accommodate different objects and modalities.

To tackle the above problems, we firstly attempt to transform the Eqn.(9) into a simpler formulation containing fewer energy weights. This goal can be achieved by merging the two terms of CV model into only one term. According to the Euler-Lagrange theorem, the energy functional of CV model can be minimized by solving the following gradient flow

$$\begin{aligned} \frac{\partial\phi_{CV}}{\partial t} &= \delta(\phi) \left[ v_1(I - c_1)^2 - v_2(I - c_2)^2 \right] \\ &= \delta(\phi)(v_1 - v_2) \left[ \frac{\sqrt{v_1}c_1 + \sqrt{v_2}c_2}{\sqrt{v_1} + \sqrt{v_2}} - I \right] \\ &\quad \times \left[ \frac{\sqrt{v_1}c_1 - \sqrt{v_2}c_2}{\sqrt{v_1} - \sqrt{v_2}} - I \right] \end{aligned} \quad (10)$$

Note that  $(\sqrt{v_1}c_1 + \sqrt{v_2}c_2) / (\sqrt{v_1} + \sqrt{v_2}) \in (c_1, c_2)$  and  $(\sqrt{v_1}c_1 - \sqrt{v_2}c_2) / (\sqrt{v_1} - \sqrt{v_2}) \notin (c_1, c_2)$ . Since we expect  $\partial\phi_{CV}/\partial t = 0$  when the zero level contour moves to the object boundary, only the term  $(\sqrt{v_1}c_1 + \sqrt{v_2}c_2) / (\sqrt{v_1} + \sqrt{v_2}) - I$  can be expected to approach to 0. Then, we can obtain the equivalent form of Eqn.(10) as

$$\frac{\partial\phi_{CVeq}}{\partial t} = v\delta(\phi)(\alpha c_1 + \beta c_2 - I) \quad (11)$$

where  $\alpha = \sqrt{v_1}/(\sqrt{v_1} + \sqrt{v_2})$  and  $\beta = \sqrt{v_2}/(\sqrt{v_1} + \sqrt{v_2})$ . Note that  $\alpha, \beta > 0$  and  $\alpha + \beta = 1$ .  $v > 0$  is a constant that controls the descent speed of the energy functional.

In this case, the equivalent energy functional of CV model can be expressed as

$$E_{CVeq}(\phi) = v \int_{\Omega} (\alpha c_1 + \beta c_2 - I)H(-\phi)d\mathbf{x} \quad (12)$$

By replacing the CV term in Eqn.(9) with its equivalent form, the energy functional  $E_H(\phi)$  can be rewritten as

$$E_H(\phi) = \lambda_1 \int_{\Omega} g\delta(\phi) |\nabla\phi| d\mathbf{x} + \lambda_2 \int_{\Omega} gH(-\phi)d\mathbf{x} + v \int_{\Omega} \text{sgn}(P_{CV})(\alpha c_1 + \beta c_2 - I)H(-\phi)d\mathbf{x} \quad (13)$$

where  $\text{sgn}$  denotes the sign function, that is, if  $P_{CV} > 0$ , then  $\text{sgn}(P_{CV}) = 1$ ; if  $P_{CV} < 0$ ,  $\text{sgn}(P_{CV}) = -1$ ; if  $P_{CV} = 0$ ,  $\text{sgn}(P_{CV}) = 0$ . The scalar  $P_{CV}$  is defined as a direction controller to ensure that the zero level contour always moves to the object boundary and the energy value of  $E_H(\phi)$  will always decrease. For CV model,  $P_{CV}$  can be defined as  $P_{CV} = c_1 - c_2$ .

In section II, it has been stated that the second term in Eqn.(1) is a driving term that drives the evolution curve to the object boundary. Since the CV term has the same ability to drive the motion of LSF, the driving term of DRLSE model can be cancelled in Eqn.(13). Then, we obtain that

$$E_H(\phi) = \lambda_1 \int_{\Omega} g\delta(\phi) |\nabla\phi| d\mathbf{x} + v \int_{\Omega} \text{sgn}(P)(\alpha c_1 + \beta c_2 - I)H(-\phi)d\mathbf{x} \quad (14)$$

Although the number of energy weight is reduced compared Eqn.(14) with Eqn.(9), it is still difficult to find out the relationship between the two terms in Eqn.(14) because their energy values might still vary greatly. Since the function  $g$  is a normalized indicator that ranges from (0, 1], we normalize the equivalent term of CV model and finally obtain that

$$E_H(\phi) = \lambda_1 \int_{\Omega} g\delta(\phi) |\nabla\phi| d\mathbf{x} + v \int_{\Omega} f_{CV}H(-\phi)d\mathbf{x} \quad (15)$$

where  $f_{CV}$  is a normalized equivalent term of CV model, which is expressed as

$$f_{CV} = \text{sgn}(P) \frac{\alpha c_1 + \beta c_2 - I}{|\alpha c_1 + \beta c_2 - I|} \quad (16)$$

In fact, the Eqn.(15) is a basic expression of our RESLS framework. Compared the Eqn.(15) with Eqn.(1), it can be seen that the change is to replace the edge indicator function  $g$  to a normalized equivalent region term  $f_{CV}$ . It seems like a small change, but indeed an important replacement. The reason is that the function  $f_{CV}$  not only embeds the region information into the edge-based model using only one term, but also acts as a driving force to drive the motion of LSF so as to avoid adding extra driving force. As a result, the number of energy weight in Eqn.(9) can be effectively reduced. Moreover, the normalization of the equivalent region term is very beneficial to quantitatively describe the relationship between region and edge information and finally deduce the global optimization condition of our RESLS framework for reliably choosing the energy weights. This will be discussed in deep in section III-C.

### B. Formulation of RESLS

In this section, we use the same mathematical notations as in section II to describe our method. The RESLS requires to define an energy functional with respect to the LSF, which is desired to achieve its global minimum when the zero level contour converges to the object boundary. Inspired by Eqn.(15), we formulate the external energy term that combines the region and edge information as below

$$E^{ext}(\phi) = \underbrace{\lambda \int_{\Omega} g\delta(\phi) |\nabla\phi| d\mathbf{x}}_{\text{edge term}} + v \underbrace{\int_{\Omega} fH(-\phi)d\mathbf{x}}_{\text{region term}} \quad (17)$$

where  $\lambda \geq 0, v > 0$  are the energy weights. The function  $g$  is the same as Eqn.(2), and  $f$  is a normalized intensity indicator function as defined in Eqn.(18). Note that it is a preliminary formulation, the final function  $f$  is defined in Eqn.(37) and will be discussed in section III-D.

$$f(\mathbf{x}) = \text{sgn}(P) \frac{\alpha f_1(\mathbf{x}) + \beta f_2(\mathbf{x}) - I(\mathbf{x})}{|\alpha f_1(\mathbf{x}) + \beta f_2(\mathbf{x}) - I(\mathbf{x})|} \quad (18)$$

In Eqn.(18),  $f_1(\mathbf{x})$  and  $f_2(\mathbf{x})$  are two functions similar to  $c_1$  and  $c_2$  in Eqn.(16). Note that they are general representations for other level set models, such as the  $u_1(\mathbf{x})$  and  $u_2(\mathbf{x})$  in Eqn.(4), etc. Constants  $\alpha, \beta > 0$  depend on the specific formulation of the level set model which is used to construct the RESLS framework and  $\alpha + \beta = 1$ . Since the denominator  $|\alpha f_1 + \beta f_2 - I|$  can not be 0, we define that if a point  $\mathbf{x}$  makes  $|\alpha f_1 + \beta f_2 - I| = 0$ , then  $f(\mathbf{x}) = 0$ . The scalar  $P$  is defined as a direction controller to ensure that the energy functional always achieves its global minimum when the zero level contour moves to the object boundary. In a general manner, the scalar  $P$  can be formulated as

$$P = \int_{\Omega} [f_1(\mathbf{x}) - f_2(\mathbf{x})] d\mathbf{x} \quad (19)$$

Similar to many existing level set models, the regularization term should be used in our method, which is defined as

$$E^{reg}(\phi) = \underbrace{\omega \int_{\Omega} \delta(\phi) |\nabla \phi| d\mathbf{x}}_{\text{length term}} + \underbrace{\mu \int_{\Omega} q(|\nabla \phi|) d\mathbf{x}}_{\text{distance term}} \quad (20)$$

where  $\omega \geq 0, \mu > 0$  are the energy weights, and  $q(|\nabla \phi|)$  denotes the double-well potential function as in Eqn.(21).

$$q(|\nabla \phi|) = \begin{cases} \frac{1}{(2\pi)^2} [1 - \cos(2\pi |\nabla \phi|)] & 0 \leq |\nabla \phi| < 1 \\ \frac{1}{2} (|\nabla \phi| - 1)^2 & |\nabla \phi| \geq 1 \end{cases} \quad (21)$$

The regularization term in Eqn.(20) consists of a length regularization term [31] and a distance regularization term [30]. The length term can be used to control the smoothness of the final evolution curve, and the distance term will intrinsically maintain the regularity of LSF during the level set evolution.

Finally, the energy functional  $E(\phi)$  of RESLS framework can be defined by combining the external energy term in Eqn.(17) and the regularization term in Eqn.(20), which is expressed as

$$E(\phi) = E^{ext}(\phi) + E^{reg}(\phi) \quad (22)$$

### C. Global Optimization Condition of RESLS

A gratifying property of RESLS framework is that, if some conditions are satisfied, it will be global optimal with regard to an arbitrarily shaped object. Suppose  $I(\mathbf{x})$  to be a homogeneous image with an arbitrarily shaped object and an infinite background, which are separated by a smooth and closed curve  $C$  (for 2D, and surface for 3D). Similar to the signed distance function that is commonly reinitialized or regularized during

the curve evolution in many level set models, we define a LSF as

$$\phi(\mathbf{x}, t) = \begin{cases} r - \text{dist}(\mathbf{x}, C) - t & \mathbf{x} \in \text{inside}(C) \\ r - t & \mathbf{x} \in C \\ r + \text{dist}(\mathbf{x}, C) - t & \mathbf{x} \in \text{outside}(C) \end{cases} \quad (23)$$

where  $r > 0$  is a constant and  $\text{dist}(\mathbf{x}, C) > 0$  denotes the shortest Euclidean distance from the point  $\mathbf{x}$  to the curve  $C$ . It can be seen from Eqn.(23) that, when  $t = r$ , then  $\phi(\mathbf{x}, t) = 0$  represents the boundary of the object  $C$ .

*Theorem: Under the above hypothesis of image  $I$ , curve  $C$ , and the LSF defined in Eqn.(23), the sufficient and necessary condition for RESLS to be global optimal is that*

$$\forall t \in (0, +\infty) : 0 \leq \frac{\lambda + \omega}{v} \leq \left| \frac{L(t)}{L'(t)} \right| \quad (24)$$

where  $L(t) \geq 0$  represents the length of zero level contour (for 2D, and the area of zero level surface for 3D) at the moment  $t$ , and  $L'(t)$  is the first derivative of  $L(t)$ .

*Proof:* From the definition of the LSF in Eqn.(23), we can easily prove that  $|\nabla \phi| = 1$ . Therefore, the distance regularization term in Eqn.(20) can be left out since  $q(|\nabla \phi|) = 0$ .

In the case that the object and background of image  $I$  are homogeneous, the function  $g = 1$  if  $\mathbf{x} \notin C$ , and  $g \rightarrow 0$  if  $\mathbf{x} \in C$ . Meanwhile,  $f_1$  and  $f_2$  represent the intensity features inside and outside the zero level contour, respectively. Since  $\alpha + \beta = 1$ , if  $P > 0$  in Eqn.(19), then  $f_1 > \alpha f_1 + \beta f_2 > f_2$ ; if  $P < 0$ , then  $f_1 < \alpha f_1 + \beta f_2 < f_2$ . Therefore, in Eqn.(18), the function  $f(\mathbf{x}) = -1$  if  $\mathbf{x} \in \text{inside}(C)$ , and  $f(\mathbf{x}) = 1$  if  $\mathbf{x} \in \text{outside}(C)$ .

Note that the first-order partial derivative of  $E(\phi)$  with respect to  $t$  can be expressed as

$$\frac{\partial E(\phi)}{\partial t} = \frac{\partial E(\phi)}{\partial \phi} \frac{\partial \phi}{\partial t} = - \frac{\partial E(\phi)}{\partial \phi} \quad (25)$$

By substituting Eqn.(23) and Eqn.(22) into Eqn.(25), the  $\partial E(\phi)/\partial t$  can be derived as

$$\frac{\partial E(\phi)}{\partial t} = \begin{cases} (\lambda + \omega)L'(t) - vL(t) & t \in (0, r) \\ (\lambda + \omega)L'(t) + vL(t) & t \in (r, +\infty) \end{cases} \quad (26)$$

where  $L(t)$  and  $L'(t)$  are respectively denoted by

$$L(t) = \int_{\Omega} \delta(\phi) |\nabla \phi| d\mathbf{x} \quad (27)$$

$$L'(t) = \int_{\Omega} \delta(\phi) \text{div} \left( \frac{\nabla \phi}{|\nabla \phi|} \right) d\mathbf{x} \quad (28)$$

It is obvious that the  $L(t) \geq 0$  represents the length of zero level contour (for 2D, and the area of zero level surface for 3D) at the moment  $t$ . In Eqn.(28),  $\text{div}(\cdot)$  is the divergence operator.  $L'(t) > 0$  and  $L'(t) < 0$  represent the expansion and shrink of the zero level contour, respectively. In the case of  $\lambda, \omega \geq 0, v > 0$ , to maintain the global optimum of  $E(\phi)$ , i.e.,  $t = r$ , the following conditions must be satisfied.

$$\begin{cases} \text{if } L'(t) > 0, \text{ then } \forall t \in (0, r) : \frac{\partial E(\phi)}{\partial t} \leq 0 \\ \text{if } L'(t) < 0, \text{ then } \forall t \in (r, +\infty) : \frac{\partial E(\phi)}{\partial t} \geq 0 \end{cases} \quad (29)$$

Then, we obtain the necessary and sufficient condition as Eqn.(24). ■

It should be stated that the condition in Eqn.(24) is satisfied only when the image  $I$  is homogeneous. However, in practice, the intensity distribution can be varied in most images, resulting in local minima of  $E(\phi)$ . The main reason is that if  $\mathbf{x} \notin C$ , the function  $g$  ranges from  $(0, 1]$  instead of  $g = 1$ . Note that the local minima can also be caused by the function  $f$ , but it is more insensitive to the fluctuation of intensity compared with  $g$  and can be ignored. In this case, the  $\partial E(\phi)/\partial t$  in Eqn.(26) can be re-derived as

$$\frac{\partial E(\phi)}{\partial t} = \begin{cases} \lambda S(t) + \omega L'(t) - v L(t) & t \in (0, r) \\ \lambda S(t) + \omega L'(t) + v L(t) & t \in (r, +\infty) \end{cases} \quad (30)$$

where  $S(t)$  is

$$S(t) = \int_{\Omega} \delta(\phi) \operatorname{div} \left( g \frac{\nabla \phi}{|\nabla \phi|} \right) d\mathbf{x} \quad (31)$$

Splitting the divergence in  $S(t)$ , it can be rewritten as

$$S(t) = \int_{\Omega} \delta(\phi) \nabla g \frac{\nabla \phi}{|\nabla \phi|} d\mathbf{x} + \int_{\Omega} \delta(\phi) g \operatorname{div} \left( \frac{\nabla \phi}{|\nabla \phi|} \right) d\mathbf{x} \quad (32)$$

In the discrete coordinate system of image  $I$ ,  $g \in (0, 1]$ , then  $|\nabla g| \in [0, \sqrt{2})$  for 2D,  $|\nabla g| \in [0, \sqrt{3})$  for 3D, and  $|\nabla g| \in [0, \sqrt{n})$  for nD. Note that  $\nabla \phi / |\nabla \phi|$  is the normalized gradient of  $\phi$ , therefore,

$$|S(t)| < \sqrt{n} |L(t)| + |L'(t)| \quad (33)$$

Similar to Eqn.(29), we can obtain the approximate condition for RESLS to be global optimal, which is shown as

$$\forall t \in (0, +\infty) : 0 \leq \frac{\lambda + \omega}{v - \sqrt{n}\lambda} \leq \left| \frac{L(t)}{L'(t)} \right| \quad (34)$$

In terms of this optimization condition, the relationship between the region and edge terms is quantitatively represented. It can be seen that the energy weights are only correlated with the length of the zero level contour  $L(t)$  and its first derivative  $L'(t)$ . In this case, the Eqn.(34) can be an important basis for selecting parameters  $\lambda$  and  $v$  in the RESLS framework. Note that the parameter  $\omega$  is set independently according to the desired smoothness of the final contour.

#### D. Smoothness of the Normalized Indicator

It is worth noting that the function  $f$  defined in Eqn.(18) is normalized, which makes it easy to derive the optimization condition as Eqn.(34), and makes it reliable to select the energy weights  $\lambda$  and  $v$ . However, it might cause undesired results when the zero level contour moves close to the object boundary. Only considering the region term in Eqn.(17), it can be minimized by solving the following gradient flow

$$\frac{\partial \phi}{\partial t} = v \delta(\phi) \operatorname{sgn}(P) \frac{\alpha f_1(\mathbf{x}) + \beta f_2(\mathbf{x}) - I(\mathbf{x})}{|\alpha f_1(\mathbf{x}) + \beta f_2(\mathbf{x}) - I(\mathbf{x})|} \quad (35)$$

Note that  $\delta(\phi) \neq 0$  only if the point  $\mathbf{x}$  is exactly located at the zero level contour. We expect  $\partial \phi / \partial t = 0$  when the contour moves to the object boundary. However, the normalized term makes it difficult to achieve this goal because any intensity

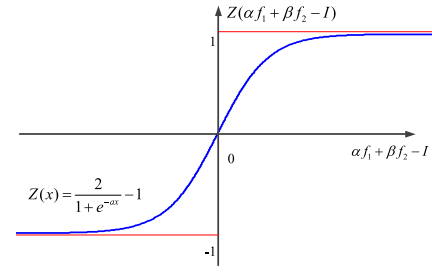


Fig. 1. The basic shape of the function  $Z$  defined in Eqn.(36). If  $(\alpha f_1 + \beta f_2 - I)$  is much different from 0, then  $Z \rightarrow \pm 1$ ; if  $(\alpha f_1 + \beta f_2 - I) \rightarrow 0$ , then  $Z \rightarrow 0$ .

value except 0 in the matrix  $(\alpha f_1 + \beta f_2 - I) / |\alpha f_1 + \beta f_2 - I|$  is normalized to 1 or -1.

To overcome this problem, we approximate the normalized term  $(\alpha f_1 + \beta f_2 - I) / |\alpha f_1 + \beta f_2 - I|$  by  $Z(\alpha f_1 + \beta f_2 - I)$ , where the function  $Z$  is defined as

$$Z(x) = \frac{2}{1 + e^{-ax}} - 1 \quad (a > 0) \quad (36)$$

Then, the final function  $f$  used in our RESLS framework can be expressed as

$$f(\mathbf{x}) = \operatorname{sgn} \left[ \int_{\Omega} [f_1(\mathbf{x}) - f_2(\mathbf{x})] d\mathbf{x} \right] \times \left[ \frac{2}{1 + \exp[-a(\alpha f_1(\mathbf{x}) + \beta f_2(\mathbf{x}) - I(\mathbf{x}))]} - 1 \right] \quad (37)$$

Fig.1 shows the basic shape of the function  $Z$ . It is obvious that if  $(\alpha f_1 + \beta f_2 - I)$  is much different from 0, then  $Z \rightarrow \pm 1$ ; if  $(\alpha f_1 + \beta f_2 - I) \rightarrow 0$ , then  $Z \rightarrow 0$ . Generally,  $Z \rightarrow 0$  only when the zero level contour is close to the object boundary. Therefore, if the evolution curve is not close to the boundary, the global optimization condition in Eqn.(24) and Eqn.(34) will not be influenced. In other words, the function  $Z$  can be used to approximate the normalized term and drive the zero level contour close to the object boundary. Then, the final result will be determined by the interaction of both region and edge information.

#### E. Generality of the Normalized Indicator

It should be emphasized that the normalized intensity indicator function  $f$  is a general expression, which is not only applicable to just one model. In fact, it can be applied to many other level set methods to construct new hybrid models. Apart from the CV model discussed in section III-A, we give more examples using the related works introduced in section II. For LBF model proposed in Ref. [41], the gradient flow of  $E_{LBF}(\phi)$  in Eqn.(4) can be derived as

$$\begin{aligned} \frac{\partial \phi_{LBF}}{\partial t} &= \delta(\phi) [\gamma_1 \int_{\Omega} K(\mathbf{x}, \mathbf{y}) |I(\mathbf{x}) - u_1(\mathbf{y})|^2 d\mathbf{y} \\ &\quad - \gamma_2 \int_{\Omega} K(\mathbf{x}, \mathbf{y}) |I(\mathbf{x}) - u_2(\mathbf{y})|^2 d\mathbf{y}] \\ &= \delta(\phi) (\gamma_1 - \gamma_2) \int_{\Omega} K(\mathbf{x}, \mathbf{y}) \\ &\quad \times \left[ \frac{\sqrt{\gamma_1} u_1(\mathbf{y}) + \sqrt{\gamma_2} u_2(\mathbf{y})}{\sqrt{\gamma_1} + \sqrt{\gamma_2}} - I(\mathbf{x}) \right] \\ &\quad \times \left[ \frac{\sqrt{\gamma_1} u_1(\mathbf{y}) - \sqrt{\gamma_2} u_2(\mathbf{y})}{\sqrt{\gamma_1} - \sqrt{\gamma_2}} - I(\mathbf{x}) \right] d\mathbf{y} \quad (38) \end{aligned}$$

Since  $[\sqrt{\gamma_1}u_1 + \sqrt{\gamma_2}u_2]/(\sqrt{\gamma_1} + \sqrt{\gamma_2}) \in (u_1, u_2)$  and  $[\sqrt{\gamma_1}u_1 - \sqrt{\gamma_2}u_2]/(\sqrt{\gamma_1} - \sqrt{\gamma_2}) \notin (u_1, u_2)$ , it can be proved that  $[\sqrt{\gamma_1}u_1 + \sqrt{\gamma_2}u_2]/(\sqrt{\gamma_1} + \sqrt{\gamma_2}) - I = 0$  is an approximate solution of  $\partial\phi_{LBF}/\partial t = 0$ . Let  $\alpha = \sqrt{\gamma_1}/(\sqrt{\gamma_1} + \sqrt{\gamma_2})$  and  $\beta = \sqrt{\gamma_2}/(\sqrt{\gamma_1} + \sqrt{\gamma_2})$ , the normalized function for LBF model can be defined as

$$f_{LBF}(\mathbf{x}) = \text{sgn} \left[ \int_{\Omega} [u_1(\mathbf{x}) - u_2(\mathbf{x})] d\mathbf{x} \right] \times \left[ \frac{2}{1 + \exp[-a(\alpha u_1(\mathbf{x}) + \beta u_2(\mathbf{x}) - I(\mathbf{x}))]} - 1 \right] \quad (39)$$

In fact, as long as the similar equivalence property as Eqn.(10) or Eqn.(38) can be derived from the level set model, the normalized function  $f$  can be obtained to construct a new hybrid model. Here, we give another more complicated example using the LSACM proposed in Ref. [43]. Based on Eqn.(6), the gradient flow of LSACM can be derived as

$$\frac{\partial\phi_{LSACM}}{\partial t} = \delta(\phi) \int_{\Omega} K(\mathbf{x}, \mathbf{y}) \left[ \log \frac{\sigma_1}{\sigma_2} + \frac{|I(\mathbf{x}) - b(\mathbf{y})m_1|^2}{2\sigma_1^2} - \frac{|I(\mathbf{x}) - b(\mathbf{y})m_2|^2}{2\sigma_2^2} \right] d\mathbf{y} \quad (40)$$

Similar to the derivation in Eqn.(38), we can obtain that

$$\begin{aligned} \frac{\partial\phi_{LSACM}}{\partial t} = & \frac{\delta(\phi)}{2\sigma_1^2\sigma_2^2} \int_{\Omega} K(\mathbf{x}, \mathbf{y}) \left[ \frac{\sigma_2}{\sigma_2 + \sigma_1} \frac{\sigma_2 - \sigma_1 A(\mathbf{y})}{\sigma_2 - \sigma_1} \right. \\ & b(\mathbf{y})m_1 + \frac{\sigma_1}{\sigma_2 + \sigma_1} \frac{\sigma_2 A(\mathbf{y}) - \sigma_1}{\sigma_2 - \sigma_1} b(\mathbf{y})m_2 - I(\mathbf{x}) \\ & \times \left[ \frac{\sigma_2}{\sigma_2 - \sigma_1} \frac{\sigma_2 + \sigma_1 A(\mathbf{y})}{\sigma_2 + \sigma_1} b(\mathbf{y})m_1 \right. \\ & \left. \left. - \frac{\sigma_1}{\sigma_2 - \sigma_1} \frac{\sigma_2 A(\mathbf{y}) + \sigma_1}{\sigma_2 + \sigma_1} b(\mathbf{y})m_2 - I(\mathbf{x}) \right] d\mathbf{y} \quad (41) \end{aligned}$$

where  $A(\mathbf{y})$  is represented by

$$A(\mathbf{y}) = \left[ 1 - \frac{2(\sigma_2^2 - \sigma_1^2)}{b(\mathbf{y})(m_1 - m_2)^2} \log \frac{\sigma_1}{\sigma_2} \right]^{\frac{1}{2}} \quad (42)$$

Then, the normalized function of LSACM model can be expressed as

$$\begin{aligned} f_{LSACM}(\mathbf{x}) &= \text{sgn} \left[ \int_{\Omega} b(\mathbf{x})(m_1 - m_2) d\mathbf{x} \right] \\ &\times \left[ \frac{2}{1 + \exp[-a(F_1(\mathbf{x}) + F_2(\mathbf{x}) - I(\mathbf{x}))]} - 1 \right] \quad (43) \end{aligned}$$

where the functions  $F_1(\mathbf{x})$  and  $F_2(\mathbf{x})$  are respectively denoted by

$$F_1(\mathbf{x}) = \frac{\sigma_2}{\sigma_2 + \sigma_1} \frac{\sigma_2 - \sigma_1 A(\mathbf{x})}{\sigma_2 - \sigma_1} b(\mathbf{x})m_1 \quad (44)$$

$$F_2(\mathbf{x}) = \frac{\sigma_1}{\sigma_2 + \sigma_1} \frac{\sigma_2 A(\mathbf{y}) - \sigma_1}{\sigma_2 - \sigma_1} b(\mathbf{y})m_2 \quad (45)$$

Both the functions in Eqn.(39) and Eqn.(43) can be applied to Eqn.(17) and the global optimization condition in Eqn.(34) can also be used to guide parameters setting for the new hybrid

models. Due to the space limitation, we can not provide all the related works in section II as examples to describe the generality of our framework. However, we have to say the RESLS is indeed a generalized method since many existing level set models, such as all the typical models described in section II, can be derived to generate the normalized function proposed in Eqn.(18).

#### F. Implementation of RESLS

As for the parameters setting and implementation of RESLS, it should be firstly declared that although the theoretical analysis of our framework is constructed in a n-dimensional space, to better display the segmentation performance, we only take the 2D images as examples. Due to the distance regularization term in Eqn.(20), the regularity of LSF during level set evolution can be intrinsically preserved. Therefore, we can initialize the LSF as a two-valued function.

$$\phi(\mathbf{x}, 0) = \begin{cases} -\rho & \mathbf{x} \in \{\phi(\mathbf{x}, 0) < 0\} \\ \rho & \mathbf{x} \in \{\phi(\mathbf{x}, 0) \geq 0\} \end{cases} \quad (46)$$

$\rho \geq 1$  is a constant, which is generally suggested to be set as  $\rho = 2$  [30].

In practice, the Heaviside function  $H$  and Dirac delta function  $\delta$  are approximated by the following smooth functions [31], [41].

$$H_{\varepsilon}(z) = \frac{1}{2} \left[ 1 + \frac{2}{\pi} \arctan \left( \frac{z}{\varepsilon} \right) \right] \quad (47)$$

$$\delta_{\varepsilon}(z) = H'_{\varepsilon}(z) = \frac{1}{\pi} \frac{\varepsilon}{\varepsilon^2 + z^2} \quad (48)$$

The parameter  $\varepsilon$  is usually set as  $\varepsilon = 1.0$ . Then, the energy functional of RESLS can be rewritten as

$$\begin{aligned} E(\phi) = & \lambda \int_{\Omega} g\delta_{\varepsilon}(\phi) |\nabla\phi| d\mathbf{x} + v \int_{\Omega} f H_{\varepsilon}(-\phi) d\mathbf{x} \\ & + \omega \int_{\Omega} \delta_{\varepsilon}(\phi) |\nabla\phi| d\mathbf{x} + \mu \int_{\Omega} q(|\nabla\phi|) d\mathbf{x} \quad (49) \end{aligned}$$

According to the Euler-Lagrange theorem, the Eqn.(49) can be minimized by solving the gradient flow as below.

$$\begin{aligned} \frac{\partial\phi}{\partial t} = & \mu \text{div} [d_q(|\nabla\phi|) \nabla\phi] \\ & + \delta_{\varepsilon}(\phi) \left[ \lambda \nabla g \frac{\nabla\phi}{|\nabla\phi|} + (\lambda g + \omega) \text{div} \left( \frac{\nabla\phi}{|\nabla\phi|} \right) + v f \right] \quad (50) \end{aligned}$$

where  $d_q$  is defined in Eqn.(51).

$$d_q(|\nabla\phi|) = \frac{q'(|\nabla\phi|)}{|\nabla\phi|} = \begin{cases} \frac{\sin(2\pi |\nabla\phi|)}{2\pi |\nabla\phi|} & 0 < |\nabla\phi| < 1 \\ 1 - \frac{1}{|\nabla\phi|} & |\nabla\phi| \geq 1 \end{cases} \quad (51)$$

where  $q(|\nabla\phi|)$  is the double-well potential function defined in Eqn.(21).

It should be stated that the function  $g$  in Eqn.(2) is easily subjected to the noise of the image. Therefore, we compute the function  $g$  using the denoised image while the function  $f$  is computed using the original image. The Gaussian kernel  $G_{\sigma}$  with  $\sigma = 1.0$  and  $3 \times 3$  mask can be used to reduce the



noise. In the discrete coordinate system, the Eqn.(50) can be solved by the iterative process of gradient descent as

$$\phi^{(n+1)} = \phi^{(n)} + \Delta t \left. \frac{\partial \phi}{\partial t} \right|_{t=t_n} \quad (52)$$

where  $\phi^{(n)}$  represents the LSF at the iteration of  $n$ , and  $\Delta t$  is the time step. In terms of Ref. [30], the option of  $\Delta t$  has to obey the Courant-Friedrichs-Lewy condition for numerical stability:  $\mu \Delta t < 1/4$ . Comprehensively considering the accuracy and efficiency, we set  $\Delta t = 1$  and  $\mu = 0.1$  in our framework.

In Eqn.(49), since  $g \in (0, 1]$ , to avoid that the energy of edge term is covered by the length regularization term,  $\omega$  is suggested to be smaller than  $\lambda$ . In this paper, we set  $\omega = k\lambda$ , where  $0 \leq k \leq 1$  is a constant. We can independently set  $k$  based on the desired smoothness of the final contour. If we expect a more smooth result, then  $k$  should be larger. By default, we set  $k = 0.2$ . In this case, from the condition in Eqn.(34), we can obtain  $0 \leq \left[ \sqrt{2} + (1+k) |L'(t)/L(t)| \right] \lambda \leq v$  for 2D images. Under the discrete condition, we approximate  $L'(t)$  by  $[L(t + \Delta t) - L(t)] / \Delta t$ . Since  $\Delta t = 1$ , then  $|L'(t)/L(t)| \approx |L(t + 1)/L(t) - 1|$ . Generally,  $L(t + 1)$  will not be much larger or smaller than  $L(t)$  after just one step of iteration, we can ignore the impact caused by  $|L'(t)/L(t)|$ . Since the Eqn.(34) is a strong constraint, and simultaneously avoid that the energy of edge term is covered by the region term, we suggest  $\lambda = 0.5v$ . Note that  $v$  is the parameter which controls the gradient descent speed of the energy functional. To avoid the iterative oscillation when the zero level contour is close to the object boundary, under the condition that  $\Delta t = 1$ , we set  $v = 2$  by default. However,  $v$  can be set much larger to reduce the iterative process if the object boundary is not too weak.

The stopping condition of RESLS can be expressed as

$$\frac{\left| \int_{\Omega} H(-\phi^{(n+1)}) d\mathbf{x} - \int_{\Omega} H(-\phi^{(n)}) d\mathbf{x} \right|}{\int_{\Omega} H(-\phi^{(n)}) d\mathbf{x}} < \tau \quad (53)$$

where  $\tau=10^{-4}$  is used to sufficiently satisfy the segmentation accuracy. The parameter  $a$  in Eqn.(36) is set as  $a = 0.04$  by experiment, which will be validated in section IV. Finally, we summarize the implementation of the proposed RESLS framework as the Algorithm 1.

#### IV. EXPERIMENTAL VALIDATION

In this section, we validate the performance of RESLS framework from three aspects including the segmentation accuracy, robustness, and computational efficiency. All the computations were implemented with MATLAB R2015b on a computer with Inter(R) Core(TM) i5-4590 CPU 3.3GHz and 4GB RAM. Unless otherwise mentioned, the parameters used in RESLS are all set as discussed in section III-F, and the parameters of contrastive models are set as the original references for fair comparison.

The segmentation accuracy was evaluated by the Dice similarity coefficient (DSC) [17], [46], which characterizes the spatial overlap between the segmentation result and ground

---

#### Algorithm 1 RESLS

---

**Input:** The image  $I$  and the desired smoothness controlling parameter  $k$ .

**Output:** The final zero level contour.

- 1: Initialize the LSF and configure all the parameters as discussed before.
  - 2: Denoise the image  $I$  by the Gaussian kernel  $G_{\sigma}$ , and compute the functions  $g$  and  $\nabla g$  using the denoised image  $G_{\sigma} * I$ .
  - 3: **Repeat**
    - 1) Use the original image  $I$  to compute the functions  $f_1$  and  $f_2$  derived from the component model of RESLS.
    - 2) Compute the function  $f$  defined in Eqn.(37).
    - 3) Compute  $\partial \phi / \partial t$  in Eqn.(50).
    - 4) Update the LSF by Eqn.(52).
  - 4: **Until** the stopping condition in Eqn.(53) is satisfied.
- 

truth.

$$DSC(V_{gt}, V_{test}) = 2 \frac{|V_{gt} \cap V_{test}|}{|V_{gt}| + |V_{test}|} \quad (54)$$

where  $V_{gt}$  is the reference gold standard (ground truth), and  $V_{test}$  is the segmentation result performed by the testing method. The value of DSC ranges from 0 to 1. The closer DSC is to 1, the higher the segmentation accuracy.

#### A. Properties of RESLS

Since the region and edge information is intrinsically combined, the RESLS enables improvements of segmentation performance compared with the models which are used to construct the framework. Firstly, we validate the robustness of RESLS using different initializations of LSF. Fig.2(a) shows four different initial positions of the zero level contour on a noisy image. Fig.2(b) and (c) give the segmentation results of DRLSE and RESLS, respectively. It is clear that the DRLSE model is easily trapped into local minima, resulting in lower segmentation accuracy. Moreover, the zero level contour must be placed inside or outside the object boundary. This leads to an inherent limitation that if the zero level contour passes through the object boundary during the level set evolution, which usually occurs on weak edges, further iteration might cause the curve to drastically move far away from the real boundary, resulting in segmentation error and low stability. This phenomenon is similar to the fourth row of Fig.2(b).

In contrast, the global optimality of RESLS can greatly improve the segmentation robustness on weak boundaries compared with DRLSE model. The segmentation result of RESLS is robust in the case of a noisy image, even if the zero level contour is placed inside, outside, or cross the boundary of the object. The DSC shown in Table I also demonstrates the robustness of RESLS. The slight difference in DSC is due to the sampling period being 5 iterations rather than 1. It should be stated that we use the equivalent term of CV model to construct the RESLS in this experiment so as to prevent the noise from being smoothed by the kernel  $K(\mathbf{x}, \mathbf{y})$ .



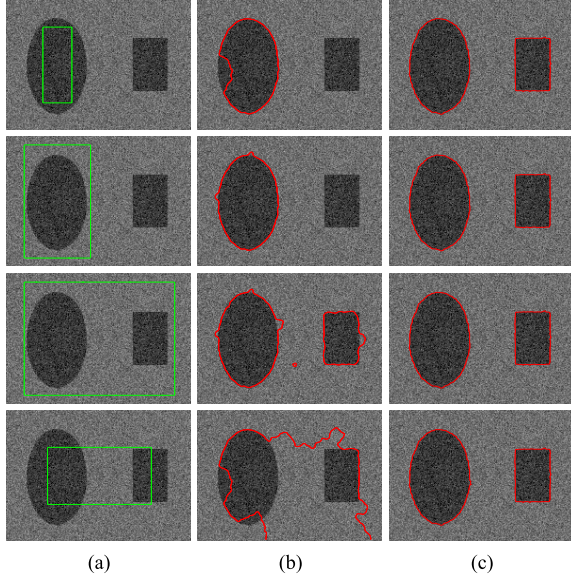


Fig. 2. The segmentation results of DRLSE and RESLS using different initializations of LSF. (a) Four different initial positions of the zero level contour. (b) The segmentation results of DRLSE. (c) The segmentation results of RESLS. The RESLS is robust to the noisy image, even if the zero level contour is inside, outside, or cross the boundary of the object.

TABLE I

COMPARISON OF SEGMENTATION ACCURACY AND COMPUTATIONAL EFFICIENCY BETWEEN RESLS AND DRLSE IN FIG.2

DRLSE			RESLS		
DSC	Iterations	Time/s	DSC	Iterations	Time/s
NA	770	2.88	0.992	100	0.41
NA	870	3.28	0.992	140	0.57
0.971	4050	15.08	0.993	180	0.74
NA	NA	NA	0.993	105	0.44

\*NA denotes not applicable.

Moreover, the computation speed of RESLS can be much faster than DRLSE in this case. Table I compares the iterations and running time between RESLS and DRLSE using the initialization of LSF as shown in Fig.2(a). It can be seen that the segmentation efficiency of RESLS can be increased more than 5 times higher than DRLSE model. In fact, the parameter  $\nu$  can be set larger under the same time step to further improve the computation speed since  $\nu$  controls the descent speed of energy functional. For example, if we set  $\nu = 3$  instead of  $\nu = 2$  in the third row of Fig.2, we can obtain the same segmentation result but the iterations and running time will be 155 and 0.65s, respectively. However, the parameter  $\nu$  should not be set too large to avoid the iterative oscillation when the zero level contour is close to the object boundary.

It is worth noting that the RESLS is also robust to the objects with intensity inhomogeneity. Let's take the LBF model as an example, which means the Eqn.(39) is used as the normalized function  $f$  for the other experiments in this subsection. Fig.3(a) shows four different initial positions of the zero level contour on an image with intensity inhomogeneity. Fig.3(b) and (c) give the segmentation results of LBF and

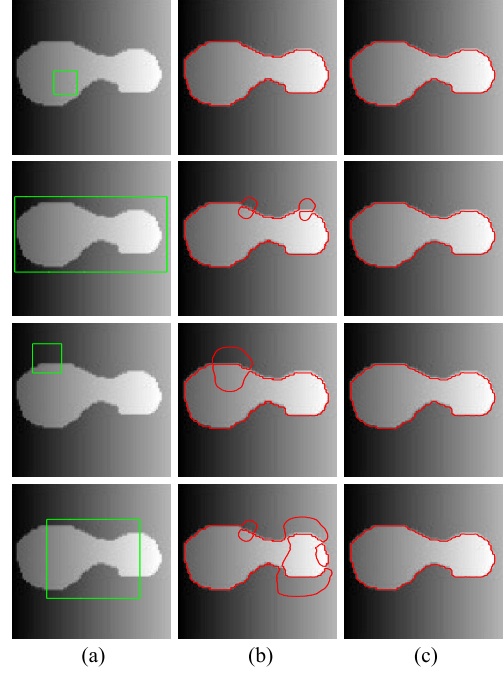


Fig. 3. The segmentation results of LBF and RESLS using different initializations of LSF. (a) Four different initial positions of the zero level contour. (b) The segmentation results of LBF. (c) The segmentation results of RESLS. The RESLS is more robust to the images with intensity inhomogeneity compared with LBF.

RESLS, respectively. It can be seen that although the LBF model achieves correct segmentation result in the first row of Fig.3(b), when the initialization of LSF changes as in the other three rows of Fig.3(a), the LBF will yield a wrong result using the same parameters. In contrast, the segmentation of RESLS is more stable in the case of different initializations of LSF.

It should be explained that the reasons of robustness in Fig.2 and Fig.3 are different. The robustness of RESLS in the noisy image is attributed to the region term that drives the motion of LSF to its global optimum. In contrast, the robustness in the image with intensity inhomogeneity is due to the edge term that forces the zero level contour to the relatively obvious object boundary. This is one of the convincing evidences which demonstrates the advantage of combining region and edge information.

Another evidence can be explained using Fig.4, which shows the segmentation results of RESLS using different parameter  $\lambda$ . To avoid the impact of the length regularization term, we set  $k = 0$ , i.e.,  $\omega = 0$  in this experiment. It can be seen from Fig.4(b) that when  $\lambda = 0$ , there are many undesired regions. With the increase of parameter  $\lambda$ , the number of undesired regions decreases, as can be seen from Fig.4(b)-(f). However, the parameter  $\lambda$  should not be too large. It can be seen from Fig.4(g) and (h) that the segmentation will be incorrect using an overlarge  $\lambda$  because the global optimization condition in Eqn.(34) will not be satisfied. To quantitatively compare the segmentation accuracy, the DSC of Fig.4 is given in Table II. Note that the RESLS obtains stable segmentation result as Fig.4(f) during  $\lambda = 0.4\nu \sim 2.9\nu$ . The DSC is no smaller than 0.987 in this range.

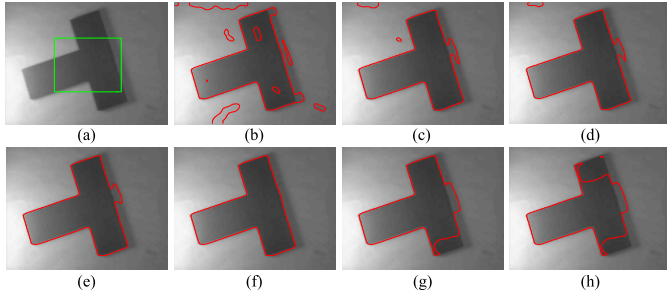


Fig. 4. The segmentation results of RESLS using different parameter  $\lambda$ . (a) The initial position of the zero level contour. (b)  $\lambda = 0$ . (c)  $\lambda = 0.1v$ . (d)  $\lambda = 0.2v$ . (e)  $\lambda = 0.3v$ . (f)  $\lambda = 0.5v$ . (g)  $\lambda = 4.0v$ . (h)  $\lambda = 5.0v$ . The number of undesired regions will be decreasing with the increase of parameter  $\lambda$ , until the global optimization condition in Eqn.(34) is unsatisfied.

TABLE II

THE SEGMENTATION ACCURACY OF RESLS USING DIFFERENT PARAMETER  $\lambda$  WITH THE LSF INITIALIZED AS FIG.4(a)

$\lambda/v$	0	0.1	0.2	0.3	0.5	4.0	5.0
DSC	0.907	0.966	0.972	0.977	0.989	0.932	0.864

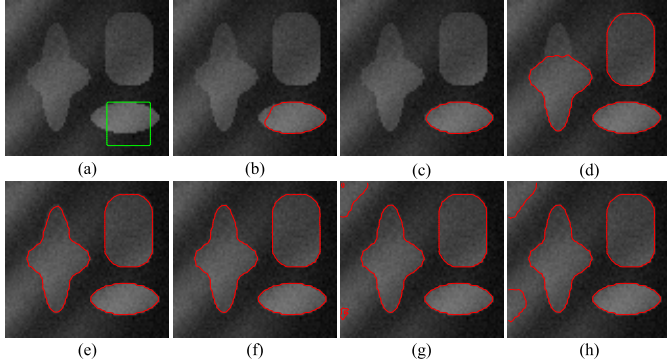


Fig. 5. The segmentation results of RESLS using different parameter  $a$  on an image with intensity inhomogeneity. (a) The initial position of the zero level contour. (b)  $a = 0.01$ . (c)  $a = 0.02$ . (d)  $a = 0.03$ . (e)  $a = 0.04$ . (f)  $a = 0.05$ . (g)  $a = 0.06$ . (h)  $a = 0.07$ . A smaller  $a$  will lead to a stronger restriction to the level set evolution. A larger  $a$  will contain more information (maybe invalid) in the segmentation result.

In the last part of this subsection, we discuss the impact of parameter  $a$  in Eqn.(36). Fig.5(b)-(h) give the segmentation results of RESLS using the parameter  $a$  from 0.01 to 0.07 on an image with intensity inhomogeneity, where the zero level contour is initialized as in Fig.5(a). It can be seen that a smaller  $a$  will lead to a stronger restriction to the level set evolution. However, a larger  $a$  will contain more information in the segmentation result, which, of course, may not be valid, as shown in Fig.5(g) and (h). The similar conclusion can be obtained from a noisy image, as with the DSC in Table III. Note that the segmentation performance directly using Eqn.(18) without being smoothed by the function  $Z$  is equivalent to the result using a large parameter  $a$  in the function  $Z$ .

In addition, the computational efficiency of RESLS can be influenced by the parameter  $a$ . Table III compares the iterations and running time using different  $a$  with the zero level contour initialized as in the fourth row of Fig.2(a). It can be seen that the RESLS suffers from low computation speed

TABLE III

THE PERFORMANCE OF RESLS USING DIFFERENT PARAMETER  $a$  WITH THE LSF INITIALIZED AS THE FOURTH ROW OF FIG.2(a)

$a$	0.001	0.005	0.01	0.05	0.1	1
DSC	0.982	0.986	0.990	0.993	0.988	0.970
Iterations	2375	430	210	90	105	115
Time/s	9.70	1.80	0.88	0.40	0.46	0.49

when  $a$  is too small because the intensity difference between the object and background is excessively reduced. Fortunately, we can obtain the best segmentation result by using a proper  $a$  and improve the computational efficiency at the same time. For instance, if we use  $a = 0.05$ , the running time will decrease over 95% for the same image, and simultaneously, we can obtain the highest accuracy of 0.993. When the parameter  $a$  is larger than 0.05, it can be seen from Table III that the computational efficiency will not increase. The reason is that the slope at zero point in the function  $Z$  will be relatively large and almost all intensity values in the matrix  $Z$  ( $\alpha f_1 + \beta f_2 - I$ ) are normalized to 1 or  $-1$ , referring to Fig.1. Comprehensively considering the intensity inhomogeneity and image noise, we set  $a = 0.04$  by default.

### B. Comparisons With the Representative Models

In this subsection, we take some practical examples to validate the segmentation performance of RESLS using some representative models, such as the DRLSE, CV, LBF, and LIC models introduced in section II. Firstly, we compare the segmentation results of RESLS with the DRLSE and CV models using the same initialization of LSF. Two lung computed tomography (CT) images (the first two rows) and a liver CT image (the last row) are used for comparison, as shown in Fig.6. Fig.6(a) shows the initial position of the zero level contour. Fig.6(b), (c) and (d) give the segmentation results of DRLSE, CV, and RESLS, respectively. It can be seen in the last two rows of Fig.6(b) that the DRLSE model is easily trapped into local minima when the intensity varies significantly. Moreover, when the weak boundary occurs as shown in the first row of Fig.6(b), the zero level contour will pass through the object during the level set evolution, and further iteration will cause the curve to drastically move far away from the object. In contrast, the RESLS is more robust to the images with irregular intensity distribution and weak boundaries compared with DRLSE, as shown in Fig.6(d). The reason is that the region term of RESLS can always drive the zero level contour to its global minimum.

For CV model, it can be seen in Fig.6(c) that there are many undesired regions caused by the intensity irregularity of the object. However, they can be reduced a lot in the proposed RESLS due to the collaboration of the edge term. This is particularly obvious in the synergetic framework that constructed by the approximately equivalent region terms of LBF and LSACM, which will be analyzed in detail afterwards. Table IV compares the DSC and running time of each method for Fig.6. It is clear that the RESLS achieves the highest segmentation accuracy. Moreover, its computational efficiency

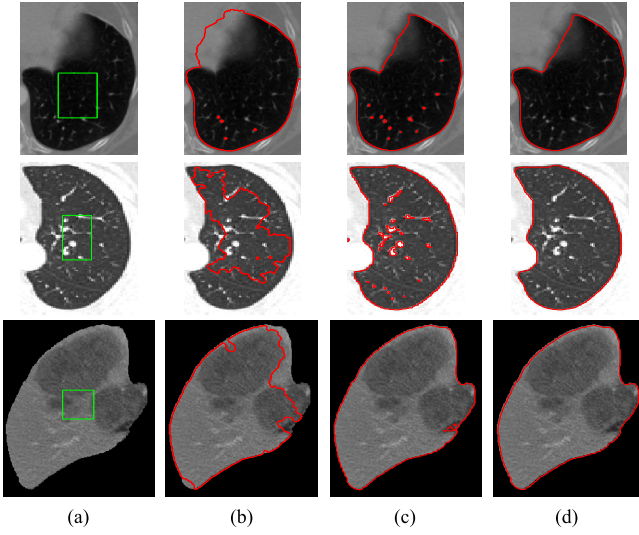


Fig. 6. Comparison of the segmentation results among DRLSE, CV, and RESLS models using the same initial LSF. (a) The initial position of the zero level contour. (b)-(d) The segmentation results of DRLSE, CV, and RESLS, respectively.

TABLE IV  
COMPARISON OF THE SEGMENTATION ACCURACY AND  
COMPUTATION TIME FOR FIG. 6

	Lung CT-1		Lung CT-2		Liver CT	
	DSC	Time/s	DSC	Time/s	DSC	Time/s
DRLSE	0.914	12.08	0.647	28.97	0.936	23.59
CV	0.973	0.61	0.975	0.95	0.994	0.27
RESLS	0.981	2.73	0.993	6.01	0.996	0.95

is much faster than that of DRLSE model, but a little slower than CV model. From this example, we can see that the RESLS framework intrinsically combines the advantages of the component models.

Next, we compare the segmentation results of RESLS with LBF model using the same initialization of LSF. As shown in Fig. 7, two magnetic resonance angiography (MRA) images (the first two rows), a brain magnetic resonance imaging (MRI) (the third row), and a heart CT image (the last row) are used for comparison. Fig. 7(a) shows the initial position of the zero level contour, and (b) shows the segmentation results of LBF. Fig. 7(c) and (d) give the segmentation results of RESLS with the parameter  $\lambda = 0$  and  $\lambda = 0.5v$ , respectively. Comparing Fig. 7(b) with (d), we can see that the RESLS is much easier to obtain satisfactory segmentation results than the LBF model. Comparing Fig. 7(c) with (d), it can be seen that the edge term is useful to reduce many undesired regions, which demonstrates the synergetic effect of region and edge information in the RESLS framework. To quantitatively compare the segmentation performance, Table V lists the DSC and running time of each case in Fig. 7. It is obvious that the RESLS achieves higher segmentation accuracy while the computation time is in the same order as LBF model.

As for the comparison with LIC model, Fig. 8 shows the segmentation results of LIC and RESLS using the same initialization of LSF, respectively. Three brain MRI images with intensity inhomogeneity are used in this experiment. Similar

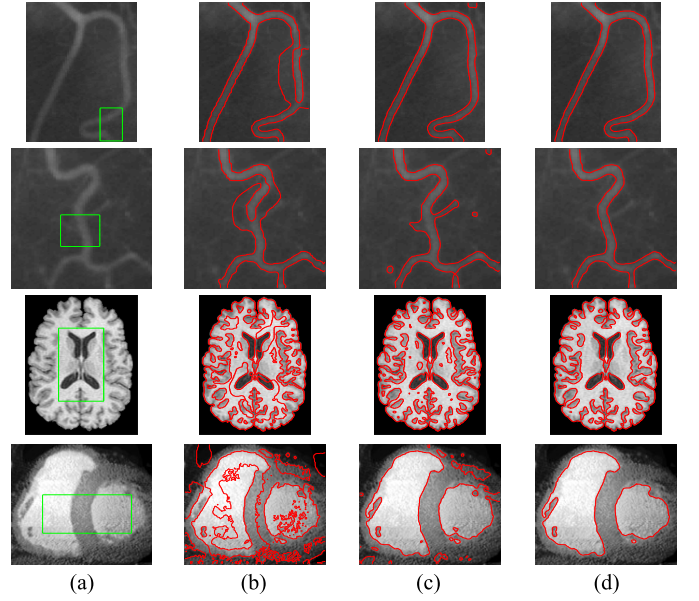


Fig. 7. The segmentation results of LBF and RESLS using the same initial LSF. (a) The initial position of the zero level contour. (b) The segmentation results of LBF model. (c)-(d) The segmentation results of RESLS with the parameter  $\lambda = 0$  and  $\lambda = 0.5v$ , respectively.

TABLE V  
COMPARISON OF THE SEGMENTATION ACCURACY AND  
COMPUTATION TIME FOR FIG. 7

	DSC		Time/s	
	MRA-1	MRA-2	Brain MRI	Heart CT
LBF	0.714	1.99	0.718	0.82
RESLS( $\lambda = 0$ )	0.963	2.11	0.906	0.88
RESLS( $\lambda = 0.5v$ )	0.984	1.94	0.978	2.76

TABLE VI  
COMPARISON OF THE SEGMENTATION ACCURACY  
AND COMPUTATION TIME FOR FIG. 8

	Brain MRI-1		Brain MRI-2		Brain MRI-3	
	DSC	Time/s	DSC	Time/s	DSC	Time/s
LIC	0.864	1.86	0.836	6.53	0.872	5.30
RESLS( $\lambda = 0$ )	0.903	1.94	0.886	8.08	0.952	5.43
RESLS( $\lambda = 0.5v$ )	0.956	1.18	0.920	12.70	0.972	4.77

to Fig. 7, it is clear that under the condition of  $\lambda = 0.5v$ , the RESLS can easily achieve more accurate segmentation results than LIC model, as can be seen from Fig. 8(b) and (d). Table VI lists the DSC and running time of each case in Fig. 8. The same conclusion can be obtained that the region and edge terms effectively work together with the guidance of the proposed optimization condition as Eqn.(34).

### C. Comparisons With State-of-the-Art Models

In this section, we further validate the performance of RESLS by comparing with some state-of-the-art models,



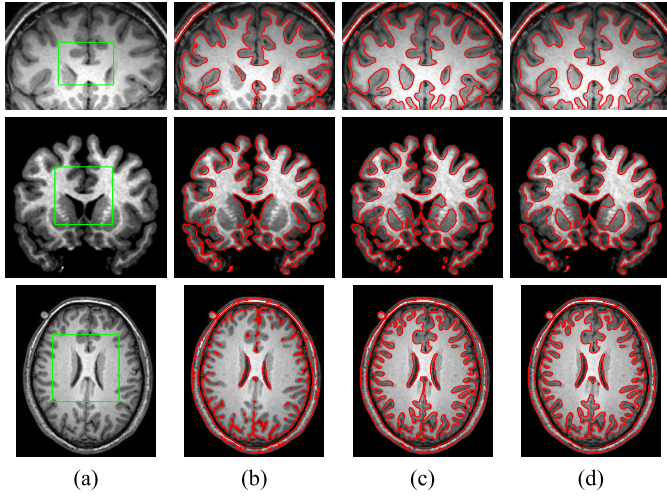


Fig. 8. The segmentation results of LIC and RESLS using the same initial LSF. (a) The initial position of the zero level contour. (b) The segmentation results of LIC model. (c)-(d) The segmentation results of RESLS with the parameter  $\lambda = 0$  and  $\lambda = 0.5v$ , respectively.

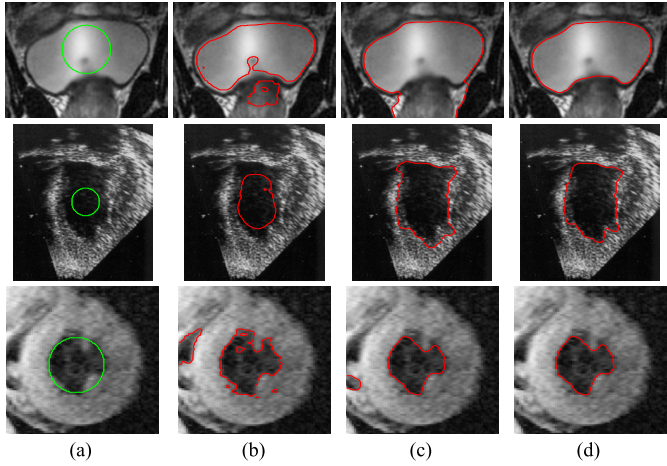


Fig. 9. The segmentation results of LSACM and RESLS using the same initial LSF. (a) The initial position of the zero level contour. (b) The segmentation results of LSACM. (c)-(d) The segmentation results of RESLS with the parameter  $\lambda = 0$  and  $\lambda = 0.5v$ , respectively.

including the LSACM, LATE and RLSF models introduced in section II. Fig.9 compares the segmentation performance between the RESLS and LSACM using a bladder MRI (the first row), a left ventricle ultrasound image (the second row), and a left ventricle MRI (the third row). Fig.9(a) shows the initial position of the zero level contour, and (b) shows the segmentation results of LSACM. Fig.9(c) and (d) give the segmentation results of RESLS with the parameter  $\lambda = 0$  and  $\lambda = 0.5v$ , respectively. It should be noted that the RESLS in this experiment is newly constructed with Eqn.(43) rather than Eqn.(37). It can be seen that the RESLS is more likely to obtain correct segmentation results than LSACM comparing Fig.9(b) with (d). Meanwhile, the region and edge information is also interacted which enables the improvement of segmentation performance, as can be seen from Fig.9(c) and (d). Table VII quantitatively compares the segmentation accuracy and running time of each case in Fig.9. It is clear

TABLE VII  
COMPARISON OF THE SEGMENTATION ACCURACY  
AND COMPUTATION TIME FOR FIG.9

	Bladder MRI		Ventricle ultrasound		Ventricle MRI	
	DSC	Time/s	DSC	Time/s	DSC	Time/s
LSACM	0.890	70.45	0.637	273.98	0.818	5.87
RESLS ( $\lambda = 0$ )	0.833	39.79	0.910	9.02	0.906	2.25
RESLS ( $\lambda = 0.5v$ )	0.985	15.16	0.964	8.57	0.954	1.72

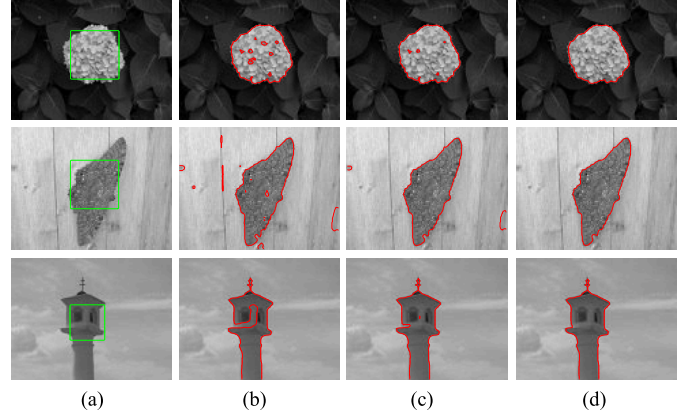


Fig. 10. The segmentation results of LATE and RESLS using the same initial LSF. (a) The initial position of the zero level contour. (b) The segmentation results of LATE. (c)-(d) The segmentation results of RESLS with the parameter  $\lambda = 0$  and  $\lambda = 0.5v$ , respectively.

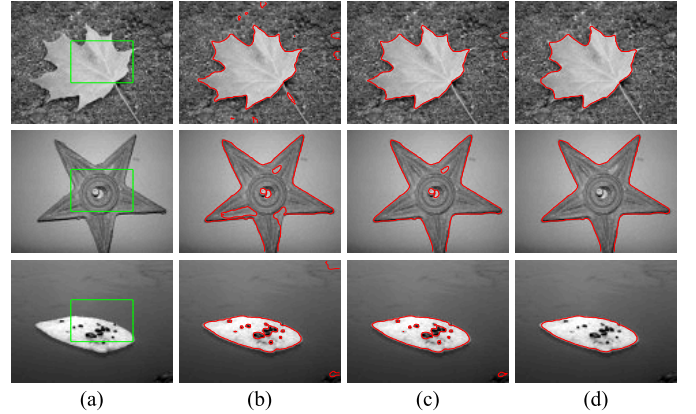


Fig. 11. The segmentation results of RLSF and RESLS using the same initial LSF. (a) The initial position of the zero level contour. (b) The segmentation results of RLSF. (c)-(d) The segmentation results of RESLS with the parameter  $\lambda = 0$  and  $\lambda = 0.5v$ , respectively.

that the RESLS outperforms the LSACM not only in accuracy but also in computational efficiency.

Analogously, we perform the comparative study with the advanced LATE and RLSF models using some natural images. For different models and parameters, the same initial zero level contour is used for each image. Fig.10 and Fig.11 illustrate the segmentation results of RESLS compared with LATE and RLSF models. Figs.10-11(a) show the initial position of



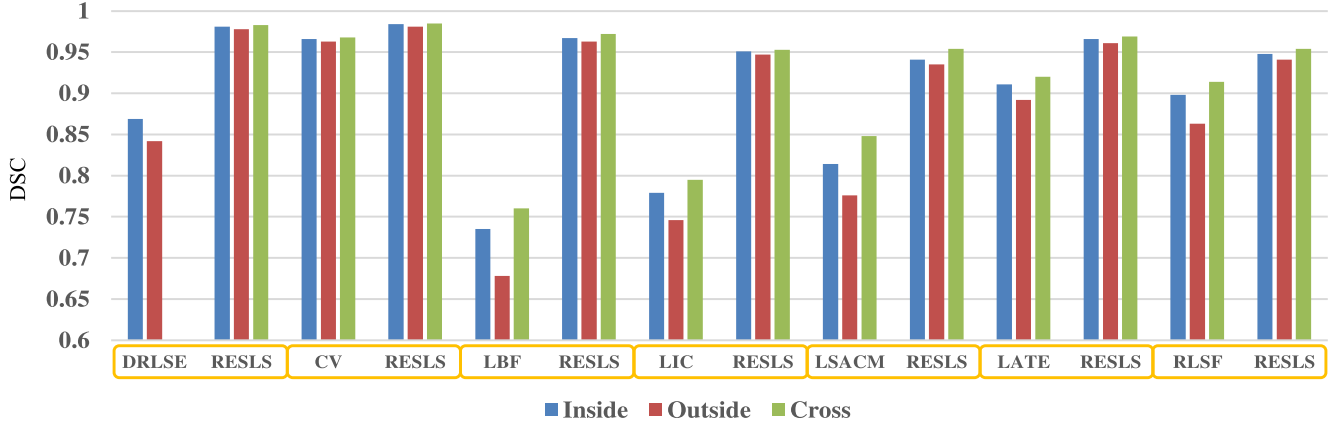


Fig. 12. The average segmentation accuracy of RESLS compared with seven representative and state-of-the-art level set models using the zero level contours inside, outside, and cross the object boundary, respectively. Note that the DRLSE model is not suitable for the cases in which the zero level contour is placed cross the object boundary.

TABLE VIII  
COMPARISON OF THE SEGMENTATION ACCURACY  
AND COMPUTATION TIME FOR FIG. 10

	Natural image-1		Natural image-2		Natural image-3	
	DSC	Time/s	DSC	Time/s	DSC	Time/s
LATE	0.963	0.93	0.935	1.55	0.954	1.25
RESLS ( $\lambda = 0$ )	0.977	0.57	0.962	1.68	0.975	1.31
RESLS ( $\lambda = 0.5v$ )	0.989	0.40	0.984	2.62	0.992	1.47

TABLE IX  
COMPARISON OF THE SEGMENTATION ACCURACY  
AND COMPUTATION TIME FOR FIG. 11

	Natural image-1		Natural image-2		Natural image-3	
	DSC	Time/s	DSC	Time/s	DSC	Time/s
RLSF	0.953	0.51	0.948	0.84	0.929	0.87
RESLS ( $\lambda = 0$ )	0.970	0.40	0.982	1.33	0.938	0.76
RESLS ( $\lambda = 0.5v$ )	0.985	0.79	0.994	1.14	0.990	0.49

the zero level contour, Figs.10-11(b) show the segmentation results of LATE and RLSF using their default parameters, Figs.10-11(c) and (d) give the segmentation results of RESLS with the parameter  $\lambda = 0$  and  $\lambda = 0.5v$ , respectively. Note that the respective equivalent region terms of LATE and RLSF are used as the component of RESLS in these experiments. Tables VIII-IX quantitatively compare the segmentation accuracy and running time of each case in Figs.10-11. It is obvious that the segmentation performance of RESLS can be improved compared with its original component models, which further demonstrates the generality of the proposed RESLS framework.

#### D. Further Evaluation

To further demonstrate the superiority of our RESLS framework, we carry out the experiment using more images with the initial zero level contour placed inside, outside, and cross the object boundary, respectively. Fig.12 shows the average DSC of RESLS compared with DRLSE, CV, LBF, LIC, LSACM, LATE, and RLSF models using 25 images for each pair. It can be validated that the RESLS is more robust to the initialization of LSF and more accurate compared with its component models. Moreover, it should be stated that the segmentation accuracy can be varied using different initial positions of LSF. The closer the initial zero level contour is to the real object boundary, the more accurate segmentation result can be obtained. Note that the DRLSE model is not suitable for the cases in which the zero level contour is placed

cross the object boundary, and the region term used in this experiment is deduced from CV model.

From the experiments above, it can be concluded that the RESLS framework can be a generalized method for constructing region and edge based hybrid level set models. The global optimization condition proposed in Eqn.(34) can be a reliable basis to choose the energy weights of region and edge terms. With the normalized intensity indicator function  $f$ , the region and edge information can be intrinsically combined, which improves the segmentation performance over the models which are used to construct the framework. Finally, it should be emphasized that although the energy weights can be chosen based on Eqn.(34), the parameters selection is not fully automatic. This is indeed one of the limitations of this work. Moreover, it has not been revealed whether the RESLS framework can be extended to multiphase level set evolution, which inspires our research in the future.

#### V. CONCLUSION

In this article, a region and edge synergetic level set framework, named RESLS, is proposed to construct hybrid active contour models with reliable energy weights. A normalized intensity indicator function is presented which allows the region information easily embedding into the edge-based model. The energy weights of region and edge terms can be chosen based on the global optimization condition deduced from the theoretical framework. The experiments with some representative and state-of-the-art models demonstrate that the

segmentation accuracy, robustness, and computational efficiency can be improved compared with the component models of RESLS. The proposed framework can be regarded as a generalized method, which might contribute to the field of hybrid active contour models.

## REFERENCES

- [1] M. Drozdal *et al.*, "Learning normalized inputs for iterative estimation in medical image segmentation," *Med. Image Anal.*, vol. 44, pp. 1–13, Feb. 2018.
- [2] C. Liu, M. K.-P. Ng, and T. Zeng, "Weighted variational model for selective image segmentation with application to medical images," *Pattern Recognit.*, vol. 76, pp. 367–379, Apr. 2018.
- [3] E. Romera, J. M. Álvarez, L. M. Bergasa, and R. Arroyo, "ERFNet: Efficient residual factorized ConvNet for real-time semantic segmentation," *IEEE Trans. Intell. Transp. Syst.*, vol. 19, no. 1, pp. 263–272, Jan. 2018.
- [4] Y. Zhang, Y. Su, J. Yang, J. Ponce, and H. Kong, "When Dijkstra meets vanishing point: A stereo vision approach for road detection," *IEEE Trans. Image Process.*, vol. 27, no. 5, pp. 2176–2188, May 2018.
- [5] B. Gao, X. Li, W. L. Woo, and G. Y. Tian, "Physics-based image segmentation using first order statistical properties and genetic algorithm for inductive thermography imaging," *IEEE Trans. Image Process.*, vol. 27, no. 5, pp. 2160–2175, May 2018.
- [6] C. Liu, Y. Xiao, and J. Yang, "A coastline detection method in polarimetric SAR images mixing the region-based and edge-based active contour models," *IEEE Trans. Geosci. Remote Sens.*, vol. 55, no. 7, pp. 3735–3747, Jul. 2017.
- [7] J. Long, E. Shelhamer, and T. Darrell, "Fully convolutional networks for semantic segmentation," in *Proc. IEEE Conf. Comput. Vis. Pattern Recognit. (CVPR)*, Jun. 2015, pp. 3431–3440.
- [8] L.-C. Chen, G. Papandreou, I. Kokkinos, K. Murphy, and A. L. Yuille, "DeepLab: Semantic image segmentation with deep convolutional nets, atrous convolution, and fully connected CRFs," *IEEE Trans. Pattern Anal. Mach. Intell.*, vol. 40, no. 4, pp. 834–848, Apr. 2017.
- [9] G. Lin, C. Shen, A. van den Hengel, and I. Reid, "Exploring context with deep structured models for semantic segmentation," *IEEE Trans. Parallel Distrib. Syst.*, vol. 40, no. 6, pp. 1352–1366, Jun. 2017.
- [10] B. Kang, Y. Lee, and T. Q. Nguyen, "Depth-adaptive deep neural network for semantic segmentation," *IEEE Trans. Multimedia*, vol. 20, no. 9, pp. 2478–2490, Sep. 2018.
- [11] J. Liu, Y. Wang, Y. Li, J. Fu, J. Li, and H. Lu, "Collaborative deconvolutional neural networks for joint depth estimation and semantic segmentation," *IEEE Trans. Neural Netw. Learn. Syst.*, vol. 29, no. 11, pp. 5655–5666, Nov. 2018.
- [12] B. Shuai, Z. Zuo, G. Wang, and B. Wang, "Scene parsing with integration of parametric and non-parametric models," *IEEE Trans. Image Process.*, vol. 25, no. 5, pp. 2379–2391, May 2016.
- [13] S. Bu, P. Han, Z. Liu, and J. Han, "Scene parsing using inference embedded deep networks," *Pattern Recognit.*, vol. 59, pp. 188–198, Nov. 2016.
- [14] R. Zhang, L. Lin, G. Wang, M. Wang, and W. Zuo, "Hierarchical scene parsing by weakly supervised learning with image descriptions," *IEEE Trans. Pattern Anal. Mach. Intell.*, vol. 41, no. 3, pp. 596–610, Mar. 2019.
- [15] H. Shi, H. Li, F. Meng, Q. Wu, L. Xu, and K. N. Ngan, "Hierarchical parsing net: Semantic scene parsing from global scene to objects," *IEEE Trans. Multimedia*, vol. 20, no. 10, pp. 2670–2682, Oct. 2018.
- [16] A. A. Kiaei and H. Khotanlou, "Segmentation of medical images using mean value guided contour," *Med. Image Anal.*, vol. 40, pp. 111–132, Aug. 2017.
- [17] A. Khadidos, V. Sanchez, and C.-T. Li, "Weighted level set evolution based on local edge features for medical image segmentation," *IEEE Trans. Image Process.*, vol. 26, no. 4, pp. 1979–1991, Apr. 2017.
- [18] Z. Liu, X. Li, P. Luo, C. C. Loy, and X. Tang, "Deep learning Markov random field for semantic segmentation," *IEEE Trans. Pattern Anal. Mach. Intell.*, vol. 40, no. 8, pp. 1814–1828, Aug. 2018.
- [19] T. H. N. Le, K. G. Quach, K. Luu, C. N. Duong, and M. Savvides, "Reformulating level sets as deep recurrent neural network approach to semantic segmentation," *IEEE Trans. Image Process.*, vol. 27, no. 5, pp. 2393–2407, May 2018.
- [20] M. Kiechle, M. Storath, A. Weinmann, and M. Kleinsteuber, "Model-based learning of local image features for unsupervised texture segmentation," *IEEE Trans. Image Process.*, vol. 27, no. 4, pp. 1994–2007, Apr. 2018.
- [21] D. Mahapatra, "Semi-supervised learning and graph cuts for consensus based medical image segmentation," *Pattern Recognit.*, vol. 63, pp. 700–709, Mar. 2017.
- [22] G. Aubert and P. Kornprobst, *Mathematical Problems in Image Processing: Partial Differential Equations and the Calculus of Variations*, vol. 147. Springer, 2006.
- [23] M. Kass, A. Witkin, and D. Terzopoulos, "Snakes: Active contour models," *Int. J. Comput. Vis.*, vol. 1, no. 4, pp. 321–331, 1988.
- [24] L. D. Cohen and I. Cohen, "Finite-element methods for active contour models and balloons for 2-D and 3-D images," *IEEE Trans. Pattern Anal. Mach. Intell.*, vol. 15, no. 11, pp. 1131–1147, Nov. 1993.
- [25] C. Xu and J. L. Prince, "Snakes, shapes, and gradient vector flow," *IEEE Trans. Image Process.*, vol. 7, no. 3, pp. 359–369, Mar. 1998.
- [26] V. Caselles, F. Catté, T. Coll, and F. Dibos, "A geometric model for active contours in image processing," *Numer. Math.*, vol. 66, no. 1, pp. 1–31, 1993.
- [27] R. Malladi, J. A. Sethian, and B. C. Vemuri, "Shape modeling with front propagation: A level set approach," *IEEE Trans. Pattern Anal. Mach. Intell.*, vol. 17, no. 2, pp. 158–175, Feb. 1995.
- [28] X. Bresson, S. Esedoğlu, P. Vanderghynst, J.-P. Thiran, and S. Osher, "Fast global minimization of the active contour/snake model," *J. Math. Imag. Vis.*, vol. 28, no. 2, pp. 151–167, Jun. 2007.
- [29] C. Li, C. Xu, C. Gui, and M. D. Fox, "Level set evolution without re-initialization: A new variational formulation," in *Proc. IEEE Comput. Soc. Conf. Comput. Vis. Pattern Recognit. (CVPR)*, vol. 1, Jun. 2005, pp. 430–436.
- [30] C. Li, C. Xu, C. Gui, and M. D. Fox, "Distance regularized level set evolution and its application to image segmentation," *IEEE Trans. Image Process.*, vol. 19, no. 12, pp. 3243–3254, Dec. 2010.
- [31] T. F. Chan and L. A. Vese, "Active contours without edges," *IEEE Trans. Image Process.*, vol. 10, no. 2, pp. 266–277, Feb. 2001.
- [32] S. Lankton and A. Tannenbaum, "Localizing region-based active contours," *IEEE Trans. Image Process.*, vol. 17, no. 11, pp. 2029–2039, Nov. 2008.
- [33] F. Mesadi, M. Çetin, and T. Taşdizen, "Disjunctive normal parametric level set with application to image segmentation," *IEEE Trans. Image Process.*, vol. 26, no. 6, pp. 2618–2631, Jun. 2017.
- [34] F. Akram, M. A. Garcia, and D. Puig, "Active contours driven by difference of Gaussians," *Sci. Rep.*, vol. 7, no. 1, Nov. 2017, Art. no. 14984.
- [35] V. Appia and A. Yezzi, "Active geodesics: Region-based active contour segmentation with a global edge-based constraint," in *Proc. Int. Conf. Comput. Vis. (ICCV)*, Nov. 2011, pp. 1975–1980.
- [36] S. Balla-Arabé, X. Gao, and B. Wang, "GPU accelerated edge-region based level set evolution constrained by 2D gray-scale histogram," *IEEE Trans. Image Process.*, vol. 22, no. 7, pp. 2688–2698, Jul. 2013.
- [37] Y. Tian, F. Duan, M. Zhou, and Z. Wu, "Active contour model combining region and edge information," *Mach. Vis. Appl.*, vol. 24, no. 1, pp. 47–61, Jan. 2013.
- [38] H. Ali, N. Badshah, K. Chen, and G. A. Khan, "A variational model with hybrid images data fitting energies for segmentation of images with intensity inhomogeneity," *Pattern Recognit.*, vol. 51, pp. 27–42, Mar. 2016.
- [39] Z. Wang and Y.-J. Liu, "Active contour model by combining edge and region information discrete dynamic systems," *Adv. Mech. Eng.*, vol. 9, no. 3, Mar. 2017, Art. no. 1687814017692947.
- [40] H. Ali, L. Rada, and N. Badshah, "Image segmentation for intensity inhomogeneity in presence of high noise," *IEEE Trans. Image Process.*, vol. 27, no. 8, pp. 3729–3738, Aug. 2018.
- [41] C. Li, C.-Y. Kao, J. C. Gore, and Z. Ding, "Implicit active contours driven by local binary fitting energy," in *Proc. IEEE Conf. Comput. Vis. Pattern Recognit. (CVPR)*, Jun. 2007, pp. 1–7.
- [42] C. Li, R. Huang, Z. Ding, J. C. Gatenby, D. N. Metaxas, and J. C. Gore, "A level set method for image segmentation in the presence of intensity inhomogeneities with application to MRI," *IEEE Trans. Image Process.*, vol. 20, no. 7, pp. 2007–2016, Jul. 2011.
- [43] K. Zhang, L. Zhang, K.-M. Lam, and D. Zhang, "A level set approach to image segmentation with intensity inhomogeneity," *IEEE Trans. Cybern.*, vol. 46, no. 2, pp. 546–557, Feb. 2016.
- [44] H. Min, W. Jia, Y. Zhao, W. Zuo, H. Ling, and Y. Luo, "LATE: A level-set method based on local approximation of Taylor expansion for segmenting intensity inhomogeneous images," *IEEE Trans. Image Process.*, vol. 27, no. 10, pp. 5016–5031, Oct. 2018.

- [45] S. Niu, Q. Chen, L. de Sisternes, Z. Ji, Z. Zhou, and D. L. Rubin, "Robust noise region-based active contour model via local similarity factor for image segmentation," *Pattern Recognit.*, vol. 61, pp. 104–119, Jan. 2017.
- [46] L. Wang, Y. Chang, H. Wang, Z. Wu, J. Pu, and X. Yang, "An active contour model based on local fitted images for image segmentation," *Inf. Sci.*, vol. 418, pp. 61–73, Mar. 2017.



**Weihang Zhang** received the B.S. degree from the School of Instrumentation Science and Opto-electronics Engineering from Beihang University, Beijing, China, in 2015. He is currently pursuing the Ph.D. degree with the Department of Precision Instrument, Tsinghua University.

His research interests include image processing, pattern recognition, and intelligent computing.



**Xue Wang** received the M.S. degree in measurement and instrument from the Harbin Institute of Technology, Harbin, China, in 1991, and the Ph.D. degree in mechanical engineering from the Huazhong University of Science and Technology, Wuhan, China, in 1994.

He was a Postdoctoral Fellow in electrical power system with the Huazhong University of Science and Technology from 1994 to 1996. He then joined the Department of Precision Instruments, Tsinghua University, Beijing, China, where he is currently a Professor and the Vice Dean. From 2001 to 2002, he was a Visiting Professor with the Department of Mechanical Engineering, University of Wisconsin–Madison. His research interests include topics in intelligent biosignal processing, wireless sensor networks, cyber physical systems, medical image processing, and 3D reconstruction.

Dr. Wang is a Senior Member of the IEEE Instrumentation and Measurement Society, Computer Society, the Computational Intelligence Society, and the Communications Society.



**Wei You** received the B.S. degree from the School of Precision Instruments and Optoelectronics Engineering, Tianjin University, Tianjin, China, in 2016. He is currently pursuing the Ph.D. degree with the Department of Precision Instrument, Tsinghua University.

His research interests include pattern recognition and intelligent computing.



**Junfeng Chen** received the B.S. degree from the Department of Precision Instrument, Tsinghua University, Beijing, China, in 2017, where he is currently pursuing the Ph.D. degree.

His research interests include image processing and edge computing.



**Peng Dai** received the B.S. degree in mechanical engineering from Tsinghua University, Beijing, China, in 2013, where he is currently pursuing the Ph.D. degree with the Department of Precision Instrument.

His research interests include image processing and video understanding.



**Pengbo Zhang** received the B.S. degree from the Department of Precision Instrument, Tsinghua University, Beijing, China, in 2014, where he is currently pursuing the Ph.D. degree.

His research interests include biosignal processing, pattern recognition, and deep learning.